

Full paper

Solubility contrast strategy for enhancing intercalation pseudocapacitance in layered MnO_2 electrodes

Yun-Pei Zhu, Chuan Xia, Yongjiu Lei, Nirpendra Singh, Udo Schwingenschlöggl, Husam N. Alshareef*

Materials Science and Engineering, Physical Science and Engineering Division, King Abdullah University of Science and Technology (KAUST), Thuwal 23955-6900, Saudi Arabia

ARTICLE INFO

Keywords:

Salt effect
Oxygen vacancy
Nanostructure control
Modified pseudocapacitance

ABSTRACT

Pseudocapacitance is generally associated with either surface redox reactions or ion intercalation processes without a phase transition. Typically, these two mechanisms have been independently studied, and most works have focused on optimizing one or the other in different material systems. Here we have developed a strategy based on solubility contrast, in which the contribution from the two capacitive mechanisms is simultaneously optimized. Taking layered birnessite MnO_2 as a model, controllable nanostructures and oxygen vacancies are achieved through a simple coprecipitation process. Simultaneously controlling crystallite size and defect concentration is shown to enhance the charging-discharging kinetics together with both redox and intercalation capacitances. This synergistic effect results from enhanced ionic diffusion, electronic conductivity, and large surface-to-volume ratio. In addition, considerable cycling durability is achieved, resulting from improved framework strength by defect creation and the absence of proton (de)intercalation during discharge/charge. This work underscores the importance of synergistically regulating nanostructure and defects in redox-active materials to improve pseudocapacitive charge storage.

1. Introduction

Capacitive energy storage features fast charging and considerable power capability, which makes it a promising energy storage technology that can complement batteries, or even replace them in certain applications [1,2]. In electrochemical capacitors, two main contributions to capacitance have been identified: (i) the double-layer capacitance is mainly a result of ion adsorption process on the surface of electrode materials (e.g., carbon nanostructures) and (ii) the pseudocapacitance results from either fast (near)surface-controlled electrochemical processes (i.e., fast redox reactions occurring at/near the surface), or rapid ion intercalation in the bulk of the electrode with no phase transition taking place in the electrode materials [3,4]. So far, the approach of most researchers has been to separately optimize either the surface redox or the intercalation pseudocapacitance. Here we present a rational electrode material design strategy, wherein both contributions to pseudocapacitance are rationally controlled.

In comparison with other polymorphs, layered or two-dimensional (2D) materials demonstrate increased capacitance and high rate behavior since the interlayer galleries can perform as highways for ion insertion and extraction during discharging and charging processes

[5–14]. This means that ion diffusion ability between each layer is strongly dependent on lateral size of the 2D materials, wherein decreasing the particle size to nanoscale region can lead to shortened diffusion path lengths, large surface-to-volume ratios, as well as abundant surface active sites, thereby ensuring an increased capacitive capability [15,16]. Accordingly, controlling the nanostructure of 2D materials provides an excellent opportunity to improve their pseudocapacitive performance [17,18]. Conventional downscaling strategies, such as electrochemical exfoliation, high-energy sonication and time-consuming ball milling, can efficiently reduce the particle size of electrode materials and elevate the capacitance to some extent, though tedious processing as well as poor control over surface defects and dimensions prohibit further improvement in capacitive performance [19,20].

As a classical capacitive electrode material used in different electrochemical devices like microsupercapacitors and (a)symmetric supercapacitors, birnessite MnO_2 has a layered structure constructed by stacked layers of edge-shared MnO_6 octahedra, thus making surface and intercalation pseudocapacitance feasible [21–26]. Nonetheless, unfavorable electronic conductivity (10^{-5} to $10^{-6} \text{ S cm}^{-1}$) and modest electrochemical kinetics pose a challenge to the widespread application

* Corresponding author.

E-mail address: husam.alshareef@kaust.edu.sa (H.N. Alshareef).<https://doi.org/10.1016/j.nanoen.2018.11.063>

Received 16 October 2018; Received in revised form 14 November 2018; Accepted 21 November 2018

Available online 24 November 2018

2211-2855/ © 2018 Published by Elsevier Ltd.

of MnO_2 . Several strategies, including heteroatom doping and hybridizing with conductive matrixes through intimate interaction [23,27–29], only offer partial solutions to compensate for the limitations of this capacitive material. On the other hand, intentionally creating defects has been confirmed to increase the charge storage capacitance of metal oxides, [30,31] in which oxygen vacancies can serve as shallow donors so as to enhance carrier concentration and electrical conduction. Several approaches like thermal annealing under the protection of inert gases, mild reduction using appropriate reductants and plasma etching have been shown to adjust the oxygen non-stoichiometry [32–34], providing a new route to enhance electrochemical performance through regulating defect chemistry in the electrode materials. Considering the critical roles of both nanostructures and defects in electrochemical energy storage, simultaneous nanostructure and defect engineering of the electrode materials is an effective strategy to enhance pseudocapacitance.

Generally, the crystal growth accompanied with oriented attachment and/or Ostwald ripening lead to a relatively high-level crystallization, leaving limited defects [35,36]. Herein, a rational design strategy based on the solubility contrast of inorganic salts in selected solvents is developed using birnessite MnO_2 as a model system. This approach intentionally impedes the crystal growth process, leading to highly defective MnO_2 . Controllable nanostructure and oxygen vacancy concentration are simultaneously realized through this coprecipitation strategy, resulting in favorable charging-discharging kinetics and cycling stability.

2. Experimental section

2.1. Synthesis of D- MnO_2

In a typical run, 4 mL of 1 mol L^{-1} NaOH ethanol solution was dropwise added to the mixed ethanol solution of 0.2 mol L^{-1} $\text{MnCl}_2 \cdot 4\text{H}_2\text{O}$ and 3.5% hydrogen peroxide under vigorous stirring. During the mixing of the two precursor solutions, the ethanol solution first turned to white (an indication of forming NaCl), followed by gradual coloration to dark brown, revealing the oxidation of divalent manganese to tetravalent manganese. The resultant homogeneous mixed solution was subjected to an additional 6 h stirring to ensure the complete reaction between the precursors. After collecting by centrifugation and drying, the as-synthesized mixture was divided into two parts, i.e., one part without further treatment, labelled as D- $\text{MnO}_2 + \text{NaCl}$ (as indicated in the XRD pattern), and other part (marked as D- MnO_2) was washed with distilled water and ethanol alternatively for several times till chloride anions could not be detected, followed by drying and collecting.

2.2. Synthesis of S- MnO_2

A totally different synthesis system was employed to prepare MnO_2 nanosheet as compared with that for defective MnO_2 . Typically, 4 mL of 1 mol L^{-1} NaOH aqueous solution was dropwise added to the mixed ethanol solution of 0.2 mol L^{-1} $\text{MnCl}_2 \cdot 4\text{H}_2\text{O}$ and 3.5% hydrogen peroxide under vigorous stirring. Different from the phenomenon observed in synthesizing D- MnO_2 , the aqueous mixture turns into dark brown immediately upon the addition of MnCl_2 solution, revealing the sole generation of MnO_2 as the result of high solubility of as-formed NaCl in water. After a 6 h stirring under ambient conditions, the product was collected by washing with water and ethanol alternatively, centrifugation and drying.

2.3. Synthesis of O- MnO_2

A further thermal treatment of the synthesized D- MnO_2 was conducted to illustrate the positive role of oxygen vacancies in enhancing capacitive performance. Generally, the D- MnO_2 sample was subjected

to an annealing process at 400°C in a muffle oven.

2.4. Physicochemical characterization

TEM and SEM images were obtained on an FEI Themis at an acceleration voltage of 200 kV and an FEI Teneo VolumeScope at high vacuum with an accelerating voltage of 5 kV, respectively. XRD patterns were collected on an X-ray diffractometer (XRD) at 40 kV and 40 mA using $\text{Co K}\alpha$ radiation (Bruker D8 ADVANCE). XPS spectra were obtained using an Axis Ultra (Kratos Analytical, UK) XPS spectrometer equipped with an Al $\text{K}\alpha$ source (1486.6 eV). A Micromeritics Autochem 2950 equipped with a thermal conductivity detector (TCD) was used to record the H_2 -TPR profiles. A certain amount of powder sample was loaded into a quartz U-shape tube, which was firstly pretreated with He (50 mL min^{-1}) at 80°C for 1 h and then cooled down to room temperature. Then a mixed gas of 10% H_2/Ar at a purging rate of 50 mL min^{-1} was introduced and the temperature was increased to 600°C at a ramp rate of $10^\circ\text{C min}^{-1}$. N_2 adsorption-desorption isotherms were collected on a Tristar II Micromeritics adsorption analyzer at -196°C and pore size distributions were calculated using the adsorption branch of the isotherms by Barrett-Joyner-Halenda (BJH) method. Raman spectra were collected on a micro-Raman spectrometer (LabRAM ARAMIS, Horiba-Jobin Yvon) with notch filters cutting at 100 cm^{-1} with the use of a Cobalt laser (633 nm, 5 mW at source).

2.5. Electrochemical testing

A classical three-electrode configuration was used to measure the electrochemical performance of the synthesized MnO_2 samples using 1 M Na_2SO_4 aqueous solution as the electrolyte, an Ag/AgCl (1 M KCl) as the reference electrode, and a platinum plate as the counter electrode. To prepare the working electrodes, the active materials, acetylene black and polyvinylidene fluoride (PVDF) at a ratio of 7:2:1 were mixed homogeneously to generate a slurry, which was then painted evenly on the carbon cloths featuring negligible capacitance. The loaded mass of active materials on the working electrode was around 2.0 mg cm^{-2} . All the electrochemical data, including cyclic voltammetry (CV), and galvanostatic charge-discharge (CD) and electrochemical impedance spectroscopy (EIS) were recorded on a Bio-Logic VMP3 multichannel potentiostat.

3. Results and discussion

In this strategy (Fig. 1), manganese chloride and sodium hydroxide ethanol solutions are mixed together under ambient condition, yielding MnO_2 and NaCl nanoparticles synchronously. Being nearly insoluble in ethanol (about 0.065 g per 100 g ethanol at room temperature), supersaturated NaCl precipitates immediately and efficiently prevents the as-generated MnO_2 crystal nuclei from further growth. This strategy prohibits the ripening process and preserves the surface defects on unsaturated MnO_2 sites (Fig. S1, Supporting information), leading to the formation of MnO_2 with particle-like crystallites (henceforth denoted as D- MnO_2). Multiple washings with water can extract the as-formed NaCl from MnO_2 easily, with masses of surface defects surviving to the final step. In sharp contrast to the synthesis in the alcohol-based system, the addition of precursors into an aqueous solution can induce the formation of single-phase, sheet-like MnO_2 with better crystallization due to the distinct solubility of NaCl in water (approximately 36 g in 100 g H_2O). The process in aqueous solution results in MnO_2 with larger crystallites, and is henceforth referred to as S- MnO_2 .

X-ray diffraction (XRD) patterns represent the mixed phase of birnessite MnO_2 and NaCl crystals for the as-prepared product using alcohol solutions (Fig. S2). In contrast, diffraction peaks coming only from MnO_2 are observed for the material prepared in aqueous solutions, indicating that a different reaction pathway takes place in different solvents. The disappearance of NaCl signals in D- MnO_2 indicates the

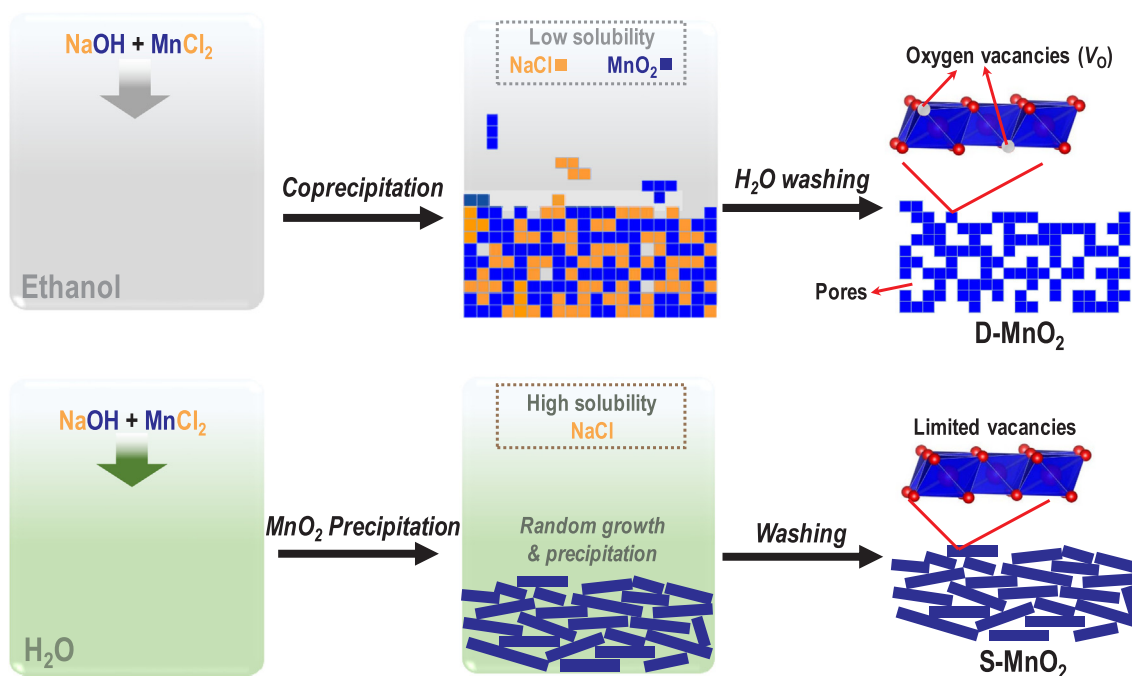


Fig. 1. Schematic illustration of synthesizing the MnO₂ electrodes with different crystallite sizes and oxygen vacancy concentrations. Mn and O atoms are shown in blue and red, respectively.

removal of inorganic salts through a simple but efficient water washing method. Unlike conventional chemical (acid or alkaline etching) and physical (acid or ethanol extraction) methods used to remove inactive hard and soft templates [37,38], the present process is much easier and is more environmentally friendly. The broader and weaker diffraction peaks observed for D-MnO₂ compared to S-MnO₂ confirm that smaller crystallite size has been achieved as a consequence of the confinement effect from co-precipitated NaCl.

Replacing ethanol with water in the synthesis process contributes to the generation of desert flower-like morphology with smooth surfaces, as illustrated by scanning (SEM) and transmission electron microscopy (TEM) images (Fig. 2a and S3). TEM image of the D-MnO₂ before removing NaCl manifests a tight assembly of nanocrystals from both materials (MnO₂ and NaCl) (Fig. S4), leaving quite limited voids or pores within the solid network. Two distinct domains, as observed in the high-resolution TEM image (HRTEM, Fig. S4), demonstrate that the NaCl and MnO₂ interlace with each other during the nanocrystal growth. In contrast, eliminating NaCl species by a subsequent washing can create a mesoporous structure with interconnected porosity (Fig. 2b). A closer observation exhibits different domains resulted from the tight aggregation of nanoparticles featuring a lattice fringe space of 0.222 nm, which is attributed to the birnessite MnO₂ (201) plane, delivering interparticle mesopores of several nanometers (Fig. 2c). Rough or stepped surfaces of the MnO₂ nanocrystallites can be intimately related to the influence of low-solubility inorganic salts on confining excessive crystallization. In stark contrast, the S-MnO₂ reference with sheet-like morphology possesses fine crystallization, smooth surface and few distinguishable defective regions (Fig. S3). A typical nitrogen sorption isotherm of type IV (Fig. 2d) with an obvious hysteresis loop confirms the well-developed mesoporosity with good connectivity. The volume of adsorbed nitrogen increases in high relative pressure region, revealing the presence of large secondary mesopores that are from the nanoparticle aggregation. Accordingly, a large surface area of 197 m² g⁻¹ can be determined for D-MnO₂, obviously exceeding S-MnO₂ (145 m² g⁻¹), which is beneficial for electrolyte infiltration and ionic transportation during electrochemical cycling.

X-ray photoelectron spectra (XPS, Fig. S5) and H₂ temperature-programmed reduction (H₂-TPR, Fig. S6) were conducted to qualify the

oxygen stoichiometry. To analyze the chemical states of manganese more accurately, the Mn 3s core-level spectra were used instead of the Mn 2p fine ones, due to the complexity of oxidation states and lack of standardization for the latter (Fig. S5). In the Mn 3s core level region (Fig. 2e), the separation of peak energies for D-MnO₂ is determined to be 5.2 eV, higher than that for S-MnO₂ (4.9 eV), suggesting that the coprecipitation strategy in ethanol can provoke the formation of more Mn³⁺, as a lower Mn valence leads to a broader splitting of the 3s peaks [17,39]. Based on the linear relationship between energy separation of the Mn 3s doublet peaks and Mn oxidation state, [40,41] the average Mn valences for D-MnO₂ and S-MnO₂ are determined to be 3.10 and 3.55, respectively, suggesting a pronounced oxygen deficiency in D-MnO₂. In addition, the deconvolution of O 1s spectra shows a primary peak at 529.7 eV (lattice oxygen) and a satellite signal at 531.6 eV (surface-chemisorbed oxygen species) (Fig. 2f), wherein the much sharper satellite for D-MnO₂ as compared with that for S-MnO₂ is indicative of a significant oxygen deficiency in D-MnO₂ [42]. In the H₂-TPR profiles (Fig. S6), two well-defined reduction peaks correspond to a stepwise reduction process, in which the first reduction signal centered at 380 °C is attributable to the reduction of MnO₂ to Mn₂O₃ and the second one in higher temperature relates to the reduction of Mn₂O₃ to MnO [43]. In comparison with the case for S-MnO₂, the less significant contribution from reducing MnO₂ to Mn₂O₃ for D-MnO₂ in the overall H₂ consumption and peak shifting to higher temperature region reveal a higher content of oxygen vacancies or trivalent manganese [44], in good accordance with the XPS results. All these results together establish that not only nanostructure and crystallite size but also oxygen vacancies can be engineered easily using this simple process. On one side, the mixed valence state (Mn⁴⁺ and Mn³⁺) can increase the electronic conductivity of manganese dioxide owing to enhanced itinerant electron mobility through forming a Mn³⁺-O-Mn⁴⁺ route [45]; on the other side, an increased electrochemical active surface area and shortened diffusion distance can be rationally realized in nanoscale electrode materials. Both features play significant roles in influencing the capacitive performance.

Cyclic voltammetry (CV) curves collected in aqueous 1 M Na₂SO₄ electrolytes feature largely rectangular shapes for the MnO₂ materials (Fig. 3a), which is characteristics of a typical capacitive behavior. The

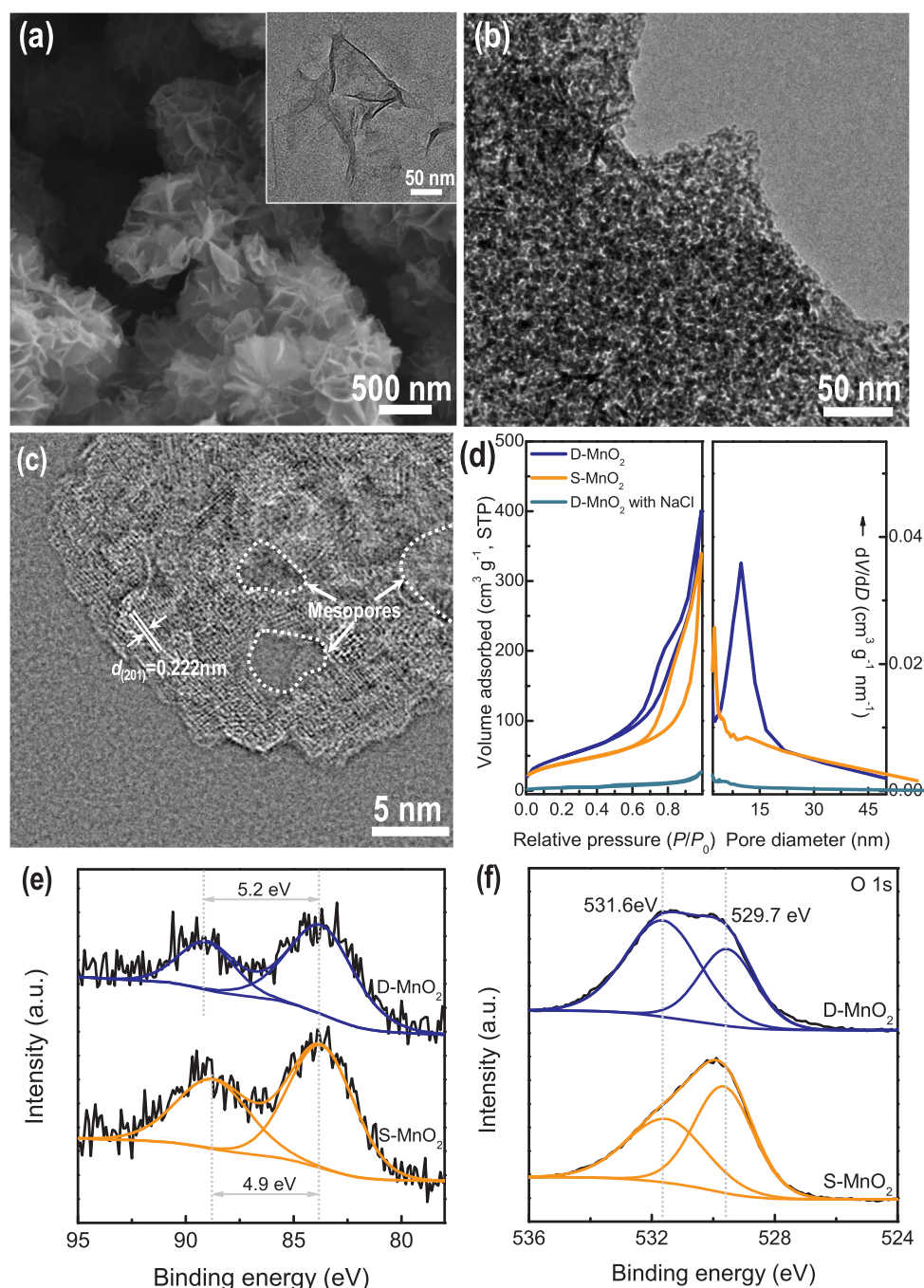


Fig. 2. (a) SEM image of S-MnO₂, with inset showing the corresponding low-resolution TEM image. (b) Low-magnification TEM and (c) aberration-corrected high-resolution TEM images of D-MnO₂. (d) N₂ sorption isotherm and corresponding pore size distribution curves of the synthesized MnO₂ materials. High-resolution (e) Mn 3s and (f) O 1s core levels of D-MnO₂ and S-MnO₂.

absence of redox peaks for S-MnO₂ implies a charging-discharging process at a fast and nearly constant rate over the whole voltammetric loop. However, the existence of wide redox peaks for D-MnO₂ suggests a detectable and active charge storage mechanism involving ion intercalation, accompanied by the electrochemical switching between Mn⁴⁺ and Mn³⁺ [17,46]. The symmetric shape of charge-discharge profiles along with a longer discharging time for D-MnO₂ (Fig. 3b) reveal a superior capacitance for D-MnO₂ compared to S-MnO₂, coinciding with the larger integrated CV area for D-MnO₂. To understand the role of oxygen vacancies in electrochemical performance, D-MnO₂ was subjected to annealing in air to decrease oxygen non-stoichiometry, and to obtain the oxidized specimen (denoted as O-MnO₂) without evident

variation in phase and morphology (Fig. S5–S7). Electrochemical results for the O-MnO₂ electrode show that thermal treatment in air reduces the capacitance and rate performance. For example, at a constant current density of 1 A g^{−1} (Fig. 3b), O-MnO₂ exhibits a gravimetric capacitance of 158 F g^{−1}, while the gravimetric capacitance of D-MnO₂ is calculated to be 202 F g^{−1}. O-MnO₂ still outperforms S-MnO₂ (112 F g^{−1} at 1 A g^{−1}) under the same testing conditions, reflecting the importance of nanostructuring in elevating capacitance [47]. Notably, the capacitive performance of D-MnO₂ is competitive or even superior to state-of-the-art MnO₂-based electrode materials, such as resembled MnO₂ nanosheet assemblies with cation vacancies (~200 F g^{−1}) [17], birnessite MnO₂ nanobelts (~150 F g^{−1}) [48], birnessite MnO₂ films

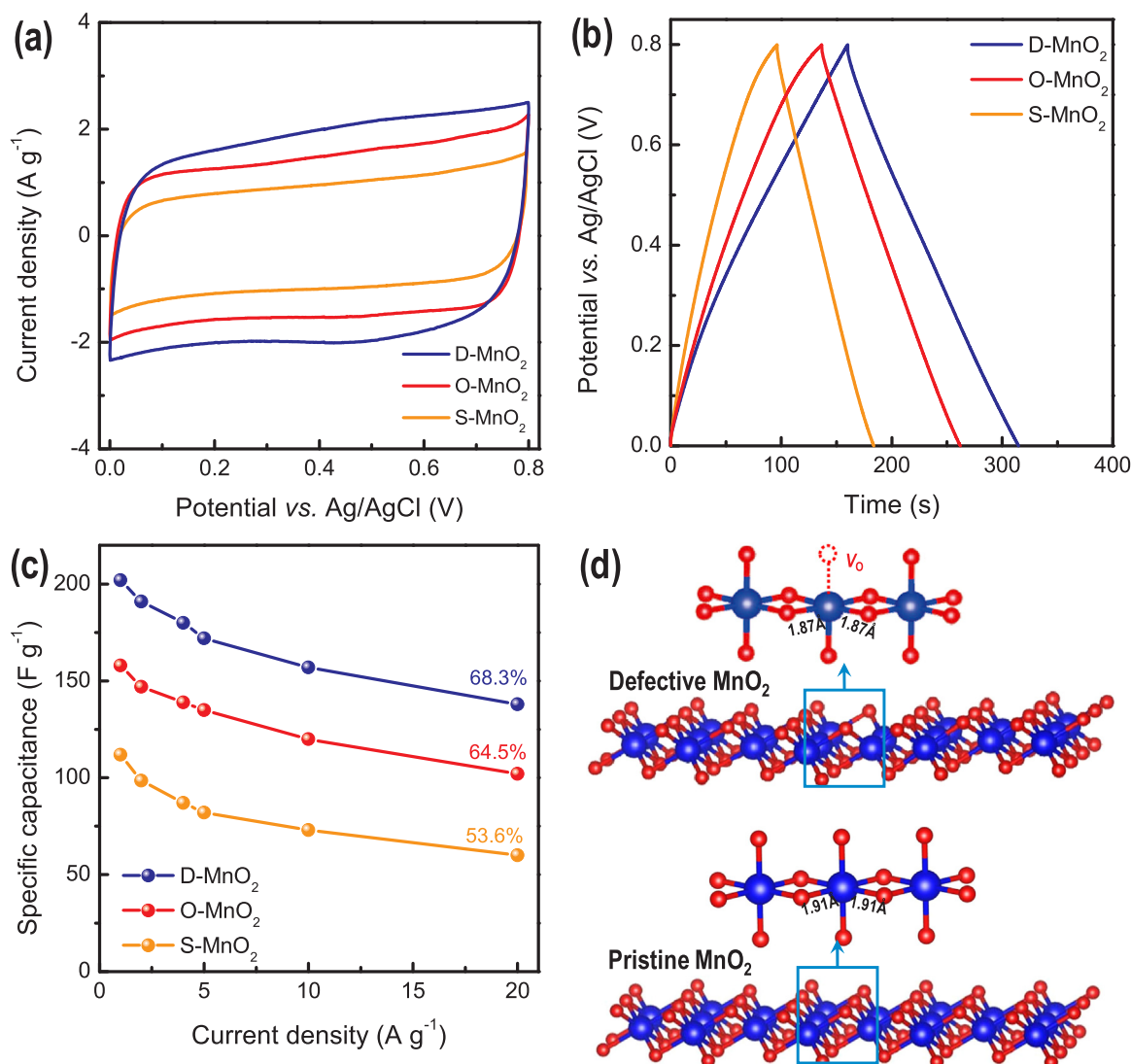


Fig. 3. (a) CV curves of the MnO₂ electrodes recorded at a scan rate of 10 mV s⁻¹. (b) Galvanostatic charge-discharge curves recorded at 1 A g⁻¹. (c) Specific capacitance comparison for the MnO₂ electrodes as a function of discharge current density. (d) Constructed models of defective and perfect birnessite MnO₂ surfaces, showing the change of the Mn-O bond length.

supported by stainless steel mesh (133 F g⁻¹) [49], MnO₂ nanostructures with a higher surface area of 201 m² g⁻¹ (110 F g⁻¹) [50], interdigital MnO₂-graphene electrodes in microsupercapacitors (249 F g⁻¹) [51], and self-assembled whisker-like MnO₂ nanoarrays (54 F g⁻¹) [52]. The specific performance decreases gradually with increasing discharge current density for the three MnO₂ samples (Fig. S8–S10), while D-MnO₂ still largely outperforms the other two control electrodes (Fig. 3c). In comparison with S-MnO₂ and O-MnO₂, the better capacitance retention with increased discharge current densities indicates a better rate capability for D-MnO₂.

The cycling test reveals that a specific capacitance decay of 10.6% is observed in the case of D-MnO₂ (Fig. S11). In contrast, the S-MnO₂ and O-MnO₂ electrodes respectively manifest 21.1% and 17.2% capacitance attenuation over the same testing duration. The stability measurements signify that introducing defects into the electrode material is a feasible way to enhance the long-term cycling stability [30,53], whereas the stability of conventional transition metal oxides used for electrochemical devices has been a significant limitation. Density functional theory (DFT) modelling (Fig. 3d) shows that introducing oxygen vacancies can reduce the Mn-O bond length, which can thus improve the Mn-O strength, as further confirmed by the shift of H₂-TPR reduction peaks to high-temperature region (Fig. S6). The increased framework

strength along with size effect of the nanoparticles and the local distortion around the oxygen vacancies are vital in relieving the electrochemical strains occurring in reversible ion intercalation/extraction processes during the cycling test, thus defining to a considerable extent of electrode stability.

Sweep voltammetry and electrochemical impedance spectroscopy (EIS) can offer deeper insights into the in electrochemical kinetics of the various electrodes. Voltammetric response demonstrates that 73% of the measured capacitance in D-MnO₂ comes from pseudocapacitive processes, while the rest is from diffusion-controlled processes (Fig. 4a and S8). In comparison, 83% of the measured capacitance in case of S-MnO₂ stems from pseudocapacitive contribution (Fig. S12). This result implies enhanced intercalation capacitance contribution after incorporating controlled nanostructure and engineered defects. Upon introducing oxygen vacancies, three new electronic states close to the Fermi level are created (Fig. 4b), resulting in an increased electronic conductivity as compared with the pristine MnO₂. From the Nyquist plots (Fig. S13), D-MnO₂ shows a much smaller semicircle diameter in high-frequency range together with a steeper line slope in the low-frequency region, confirming the improved electrical conductivity after introducing oxygen vacancies and accelerated ionic diffusion due to abundant porosity delivered by the nanoparticle assembly [54,55].

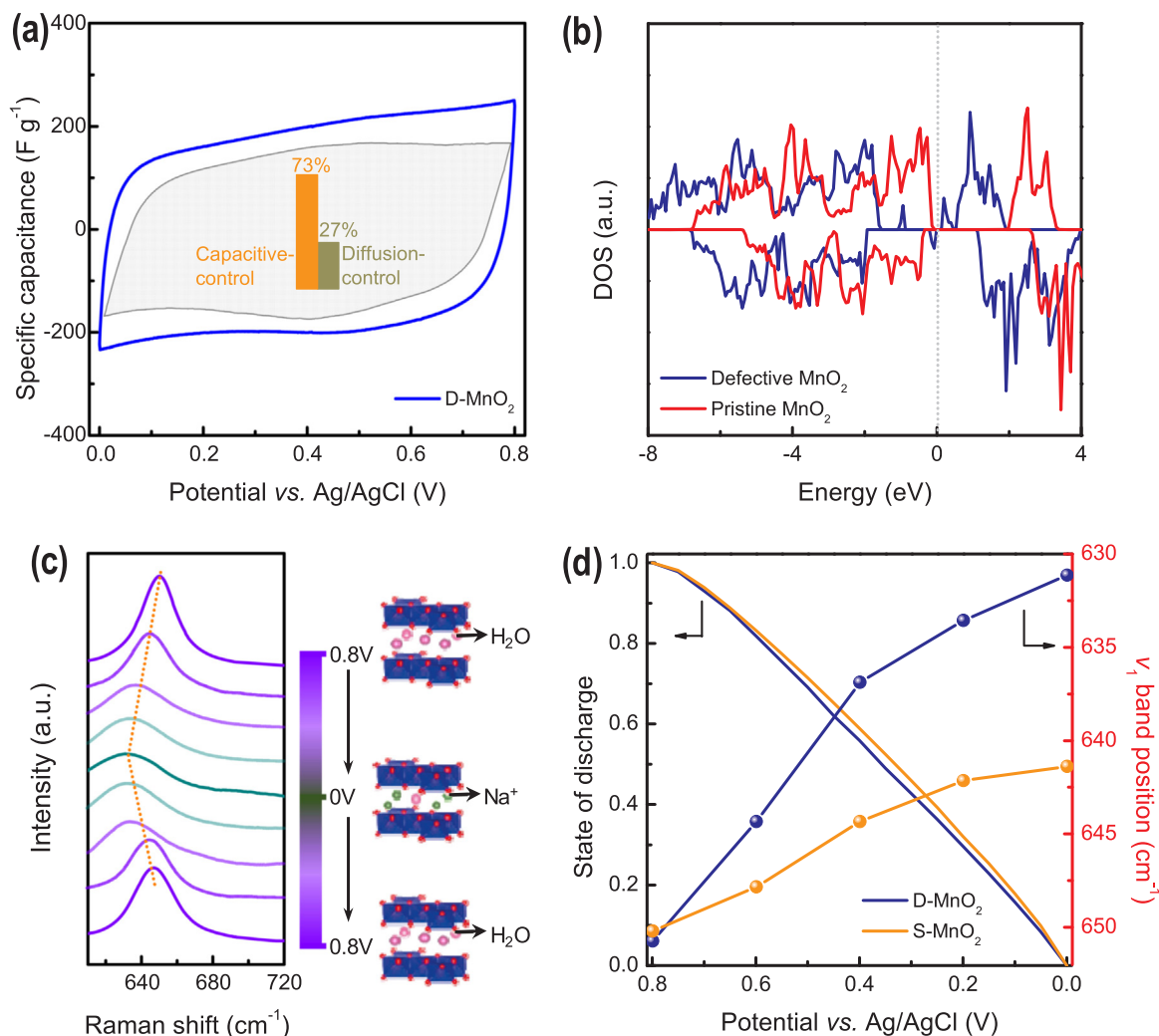


Fig. 4. (a) Kinetics analysis of the D-MnO₂ sample at a scan rate of 10 mV s⁻¹ with the grey area showing the contribution from capacitive current. (b) Projected density of states (DOS) for the MnO₂ electrodes. (c) The evolution of Raman spectrum of the capacitive D-MnO₂ electrode when the working potential is cycled between 0.8, 0, and 0.8 V; the dashed line indicates the shifting of ν_1 band position. Additionally, the schemes of water-intercalated MnO₂ and Na⁺-intercalated MnO₂ correspond to the charged state (high potential) and the discharged state (low potential), respectively. (d) Raman spectroscopic features (peak positions of ν_1 band) of D-MnO₂ and S-MnO₂ electrodes plotted against working potential during discharging process, with the state of discharge (SOD) plots correlated with the spectroscopic features.

Due to the high sensitivity of Raman spectroscopy in detecting structural variation, *ex-situ* Raman spectroscopic evolution of the D-MnO₂ model electrode during charging and discharging was investigated to further shed light on the charge storage mechanism. In the Raman spectra (Fig. 4c), the position of ν_1 band, characteristic of symmetric Mn–O stretching vibration in MnO₆ octahedral, has a positive correlation with the interlayer distance [56]. During the cathodic process, Na⁺ ions are progressively inserted into the interlayer space. For the discharging states, the substitution of smaller Na⁺ (0.099 nm) in place of the larger H₂O (0.28 nm) causes the contraction of interlayer spacing because of growing electrostatic interaction and less steric hindrance, the overall effect of which is the red shift of ν_1 band as the working potential gradually approaches 0 V. Noticeably, the insertion/extraction process is of high reversibility as the characteristic signal returns to the original states upon potential reversal. Two additional features in the Raman spectrum can be observed: the absence of any new bands, which suggests that no new species or phases are formed during the cathodic or anodic processes (Fig. S14), a hallmark of pseudocapacitance; the gradual widening of ν_1 band is assigned to the increased Jahn–Teller distortion upon Na⁺ intercalation and electron injection during the discharging process. The cation intercalation effect

can be qualified as a function of the electrochemical charge storage, rendering a systematic relationship of changes of the polarizability of the vibrational modes (ν_1 band locations and intensities) with discharging extent induced by the cation incorporation from the electrolyte, affecting the charge density distribution within the MnO₂ structure. The fraction of Na⁺ inserted into MnO₂ interlayer space can be depicted by the state of discharge (SOD) that is calculated from the integration of CV curves. Upon plotting the SOD and ν_1 band position as a function of working potential (Fig. 4d), a convex shape of SOD curve can be observed due to the deviation from ideal capacitive behavior. Distinct from the S-MnO₂ control electrode featuring less variation in terms of ν_1 band position and intensity (Fig. S15), D-MnO₂ shows a pronounced change since its charge storage mechanism is improved by the intercalation process. Such experimental observations match well with the result that reducing MnO₂ size down to several nanometers delivers a high surface-volume ratio and shortens diffusion pathways, which improves the ability to accommodate ions and enhance the overall kinetics and stability of the capacitive energy storage process. In parallel, the high-concentration Mn³⁺ cations (under-coordinated MnO₆ octahedron), which presumably contribute to polaron hopping conduction, enhance the charge transfer efficiency and electronic

conductivity (Fig. 4b) [57]. As such, the synergistic effects of defect engineering and nanostructure control can together redefine the charge transfer resistance and capacitive behavior.

The aforementioned *ex-situ* Raman results suggest that Na^+ intercalation/deintercalation contributes to the energy storage process for D-MnO_2 without phase change. XPS analysis offers further proof for the change of chemical states of the MnO_2 electrodes during charge and discharge (Fig. S16). A doublet and a peak splitting should usually appear in the Mn 3s core level region, which is a result of parallel spin coupling of 3s electron and 3d electron during the photoelectron ejection. Importantly, the energy difference between the doublet peaks is associated with the average manganese oxidation states. A lower valence relates to more electrons in 3d orbital, thus more interaction can happen upon photoelectron ejection. Upon Na^+ insertion (discharge process), the energy separation increases, indicating the decrease of manganese valences. An inverse trend is observed during charging process along with electrochemical oxidation of Mn. Noticeably, the binding energy separation of Mn 3s doublet peaks coincides with those expected for Mn^{3+} and Mn^{4+} oxides, [58] implying that the pseudocapacitive charge storage on the MnO_2 electrodes involves the valance switching between Mn^{3+} and Mn^{4+} upon sodiation and desodiation, respectively. The less significant change of Mn–OH signals indicates the absence of proton intercalation process that can produce intermediate phase MnOOH , while MnOOH is an unstable phase which can easily evolve into soluble Mn^{2+} and MnO_2 [59]. This irreversible process is usually responsible for capacitance decaying of the MnO_2 -based electrodes [60,61]. The prohibition of MnOOH disproportionation reaction, reversible structural change of the MnO_2 electrodes during cycling and enhanced framework stability after introducing oxygen vacancies are significant to realize exceptional cyclic stability. Accordingly, all the *ex-situ* Raman and XPS data are in agreement with the continuous and reversible changes of structural evolution and manganese oxidation states through switching potential between 0 and 0.8 V.

4. Conclusions

A simple and efficient strategy involving alcohol systems was proposed to synthesize defective MnO_2 nanostructures, wherein coprecipitated NaCl species could restrict MnO_2 crystallization and preserve abundant surface defects. The simultaneous control over MnO_2 morphology (nanocrystal *versus* sheets) and surface defect (oxygen vacancy) non-stoichiometry led to faster ionic diffusion processes, increased charge transfer rate, and enhanced intercalation pseudocapacitive contribution, ensuring the improved overall MnO_2 electrode performance. Through changing the precursors and synthetic parameters in the synthesis systems, our process based on solubility contrast presents a feasible way to design a wide range of active electrodes materials (e.g., metal oxides or sulfides and even multicomponent compounds) with readily controllable structures and surface defects to improve pseudocapacitive charge storage.

Acknowledgements

Research reported in this publication was supported by King Abdullah University of Science and Technology (KAUST).

Conflict of interest

The authors declare no competing financial interest.

Appendix A. Supporting information

Supplementary data associated with this article can be found in the online version at doi:10.1016/j.nanoen.2018.11.063.

References

- [1] Y. Gogotsi, R.M. Penner, ACS Nano 12 (2018) 2081–2083.
- [2] Y. Zhang, M. Xie, V. Adamaki, H. Khanbarez, C.R. Bowena, Chem. Soc. Rev. 46 (2017) 7757–7786.
- [3] P. Simon, Y. Gogotsi, B. Dunn, Science 343 (2014) 1210–1211.
- [4] V. Augustyn, P. Simon, B. Dunn, Energy Environ. Sci. 7 (2014) 1597–1614.
- [5] E. Pomerantseva, Y. Gogotsi, Nat. Energy 2 (2017) 17089.
- [6] M.R. Lukatskaya, S. Kota, Z. Lin, M.Q. Zhao, N. Shpigel, M.D. Levi, J. Halim, P.L. Taberna, M.W. Barsoum, P. Simon, Y. Gogotsi, Nat. Energy 2 (2017) 17105.
- [7] B. Deng, T. Lei, W. Zhu, L. Xiao, J. Liu, Adv. Funct. Mater. 28 (2018) 1704330.
- [8] S. Fleischmann, D. Leistenschneider, V. Lemkova, B. Krüner, M. Zeiger, L. Borchardt, V. Presser, Chem. Mater. 29 (2017) 8653–8662.
- [9] M. Acerce, D. Voiry, M. Chhowalla, Nat. Nanotechnol. 10 (2015) 313–318.
- [10] X. Yu, S. Yun, J.S. Yeon, P. Bhattacharya, L. Wang, S.W. Lee, X. Hu, H.S. Park, Adv. Energy Mater. 8 (2018) 1702930.
- [11] J. Liu, J. Wang, X. Xu, H. Jiang, C. Li, L. Zhang, J. Lin, Z. Shen, Adv. Sci. 5 (2018) 1700322.
- [12] H.J. Lee, J. Shin, J.W. Choi, Adv. Mater. 30 (2018) 1705851.
- [13] D. Chao, C.H. Lai, P. Liang, Q. Wei, Y.S. Wang, R. Zhu, G. Deng, V.V.T. Doan-Nguyen, J. Lin, L. Mai, H.J. Fan, B. Dunn, Z.X. Shen, Adv. Energy Mater. 8 (2018) 1800058.
- [14] G. Jia, D. Chao, N.Y. Tiej, Z. Zhang, H.H. Fan, Energy Storage Mater. 14 (2018) 136–142.
- [15] E. Martínez-Periñán, M.P. Down, C. Gibaja, E. Lorenzo, F. Zamora, C.E. Banks, Adv. Energy Mater. 8 (2018) 1702606.
- [16] C. Chen, Y. Wen, X. Hu, X. Ji, M. Yan, L. Mai, P. Hu, B. Shan, Y. Huang, Nat. Commun. 6 (2015) 6929.
- [17] P. Gao, P. Metz, T. Hey, Y. Gong, D. Liu, D. Edwards, J.Y. Howe, R. Huang, S.T. Mixture, Nat. Commun. 8 (2017) 14559.
- [18] J. Liu, J. Wang, C. Xu, H. Jiang, C. Li, L. Zhang, J. Lin, Z.X. Shen, Adv. Sci. 5 (2018) 1700322.
- [19] F. Li, M. Xue, X. Zhang, L. Chen, G.P. Knowles, D.R. MacFarlane, J. Zhang, Adv. Energy Mater. 8 (2018) 1702794.
- [20] F. Bonaccorso, L. Colombo, G. Yu, M. Stoller, V. Tozzini, A.C. Ferrari, R.S. Ruoff, V. Pellegrini, Science 347 (2015) 1246501.
- [21] Z. Ye, T. Li, G. Ma, Y. Dong, X. Zhou, Adv. Funct. Mater. 27 (2017) 1704083.
- [22] Y.Q. Li, X.M. Shi, X.Y. Lang, Z. Wen, J.C. Li, Q. Jiang, Adv. Funct. Mater. 26 (2016) 1830–1839.
- [23] N. Liu, Y. Su, Z. Wang, Z. Wang, J. Xia, Q. Chen, Z. Zhao, Q. Li, F. Geng, ACS Nano 11 (2017) 7879–7888.
- [24] K.W. Nam, S. Kim, S. Lee, M. Salama, I. Shterenberg, Y. Gofer, J.S. Kim, E. Yang, C.S. Park, J.S. Kim, S.S. Lee, W.S. Chang, S.G. Doo, Y.N. Jo, Y. Jung, D. Aurbach, J.K. Choi, Nano Lett. 15 (2015) 4071–4079.
- [25] C. Zhu, L. Yang, J.K. Seo, X. Zhang, S. Wang, J.W. Shin, D. Chao, H. Zhang, Y.S. Meng, H.J. Fan, Mater. Horiz. 4 (2017) 415–422.
- [26] K.W. Nam, S. Kim, E. Yang, Y. Jung, E. Levi, D. Aurbach, J.W. Choi, Chem. Mater. 27 (2015) 3721–3725.
- [27] J. Kang, A. Hirata, L. Kang, X. Zhang, Y. Hou, L. Chen, C. Li, T. Fujita, K. Akagi, M. Chen, Angew. Chem. Int. Ed. 52 (2013) 1664–1667.
- [28] M.B. Sassin, C.N. Chervin, D.R. Rolison, J.W. Long, Acc. Chem. Res. 46 (2013) 1062–1074.
- [29] P. Canepa, G.S. Gautam, D.C. Hannah, R. Malik, M. Liu, K.G. Gallagher, K.A. Persson, G. Ceder, Chem. Rev. 27 (2017) 4287–4341.
- [30] H.S. Kim, J.B. Cook, H. Lin, J.S. Ko, S.H. Tolbert, V. Ozolins, B. Dunn, Nat. Mater. 16 (2017) 454–460.
- [31] Y. Xu, M. Zhou, X. Wang, C. Wang, L. Liang, G. Grote, M. Wu, Y. Mi, Y. Lei, Angew. Chem. Int. Ed. 54 (2015) 8768–8771.
- [32] J. Ahn, J.H. Kim, B.W. Cho, K.Y. Chung, S. Kim, J.W. Choi, S.H. Oh, Nano Lett. 17 (2017) 7869–7877.
- [33] R. Liu, L. Ma, G. Niu, X. Li, W. Li, Y. Bai, G. Yuan, Adv. Funct. Mater. 27 (2017) 1701635.
- [34] A. Neumüller, O. Sergeev, S.J. Heise, S. Bereznev, O. Volobueva, J.F.L. Salas, M. Vehse, C. Agert, Nano Energy 43 (2018) 228–235.
- [35] W. Jia, Y. Liu, P. Hu, R. Yu, Y. Wang, L. Ma, D. Wang, Y. Li, Chem. Commun. 51 (2015) 8817–8820.
- [36] F.D. Ott, A. Riedinger, D.R. Ochsenein, P.N. Knüsel, S.C. Erwin, M. Mazzotti, D.J. Norris, Nano Lett. 17 (2017) 6870–6877.
- [37] J.K. Shon, H.S. Lee, G.O. Park, J. Yoon, E. Park, G.S. Park, S.S. Kong, M. Jin, J.M. Choi, H. Chang, S. Doo, J.M. Kim, W.S. Yoon, H. Pak, H. Kim, G.D. Stucky, Nat. Commun. 7 (2016) 11049.
- [38] J.C. Wang, S.P. Hill, T. Dilbeck, O.O. Ogunsolu, T. Banerjee, K. Hanson, Chem. Soc. Rev. 47 (2018) 104–148.
- [39] M. Chigane, M. Ishikawa, J. Electrochem. Soc. 147 (2000) 2246–2251.
- [40] X. Peng, Y. Guo, Q. Yin, J. Wu, J. Zhao, C. Wang, S. Tao, W. Chu, C. Wu, Y. Xie, J. Am. Chem. Soc. 139 (2017) 5242–5248.
- [41] W. Yang, Y. Zhu, F. You, L. Yan, Y. Ma, C. Lu, P. Gao, Q. Hao, W. Li, Appl. Catal. B: Environ. 233 (2018) 184–193.
- [42] F. Cheng, J. Shen, B. Peng, Y. Pan, Z. Tao, J. Chen, Nat. Chem. 3 (2011) 79–84.
- [43] D. Delimaris, T. Ioannides, Appl. Catal. B: Environ. 84 (2008) 303–312.
- [44] F. Cheng, T. Zhang, Y. Zhang, J. Du, X. Han, J. Chen, Angew. Chem. Int. Ed. 52 (2013) 2474–2477.
- [45] S. Zhu, L. Li, J. Liu, H. Wang, T. Wang, Y. Zhang, L. Zhang, R.S. Ruoff, F. Dong, ACS Nano 12 (2018) 1033–1042.
- [46] Q. Qu, L. Li, S. Tian, W. Guo, Y. Wu, R. Holze, J. Power Sources 195 (2010)

- 2789–2794.
- [47] J. Wang, J. Polleux, J. Lim, B. Dunn, *J. Phys. Chem. C* 111 (2007) 14925–14931.
- [48] P. Xiong, R. Ma, N. Sakai, X. Bai, S. Li, T. Sasaki, *ACS Appl. Mater. Interfaces* 9 (2017) 6282–6291.
- [49] W. Liu, Z. Wang, Y. Su, Q. Li, Z. Zhao, F. Geng, *Adv. Energy Mater.* 7 (2017) 1602834.
- [50] W. Chen, R.B. Rakhi, Q. Wang, M.N. Hedhili, H.N. Alshareef, *Adv. Funct. Mater.* 24 (2014) 3130–3143.
- [51] L. Peng, X. Peng, B. Liu, C. Wu, Y. Xie, G. Yu, *Nano Lett.* 13 (2013) 2151–2157.
- [52] Y. Luo, J. Jiang, W. Zhou, H. Yang, J. Luo, X. Qi, H. Zhang, D.Y.W. Yu, C.M. Li, T. Yu, *J. Mater. Chem.* 22 (2012) 8634–8640.
- [53] D.S. Sun, Y.H. Li, Z.Y. Wang, X.P. Cheng, S. Jaffer, Y.F. Zhang, *J. Mater. Chem. A* 4 (2016) 5198–5520.
- [54] M. Salanne, B. Rotenberg, K. Naoi, K. Kaneko, P.L. Taberna, C.P. Grey, B. Dunn, P. Simon, *Nat. Energy* 1 (2016) 16070.
- [55] Y. Song, T. Liu, B. Yao, M. Li, T. Kou, Z.H. Huang, D.Y. Feng, F. Wang, Y. Tong, X.X. Liu, Y. Li, *ACS Energy Lett.* 2 (2017) 1752–1759.
- [56] D. Chen, D. Ding, X. Li, G.H. Waller, X. Xiong, M.A. El-Sayed, M. Liu, *Chem. Mater.* 27 (2015) 6608–6619.
- [57] W. Wei, X. Cui, W. Chen, D.G. Ivey, *Chem. Soc. Rev.* 40 (2011) 1697–1721.
- [58] M. Toupin, T. Brousse, D. Bélanger, *Chem. Mater.* 16 (2004) 3184–3190.
- [59] L. Yang, S. Cheng, J. Wang, X. Ji, Y. Jiang, M. Yao, P. Wu, M. Wang, J. Zhou, M. Liu, *Nano Energy* 30 (2016) 293–302.
- [60] K. Nishimura, T. Douzono, M. Kasai, H. Andou, Y. Muranaka, Y. Kozono, *J. Power Sources* 81 (1999) 420–424.
- [61] L. Yang, S. Cheng, X. Ji, Y. Jiang, J. Zhou, M. Liu, *J. Mater. Chem. A* 3 (2015) 7338–7344.